Supplementary Information (SI) for ChemComm.
This journal is © The Royal Society of Chemistry 2026

Supporting information

for

Cu-Co Synergy Enabling Efficient Tandem Nitrate Reduction to Ammonia on Engineered TiO_2 Nanofibers

Bingyan Shi,[a] Haoxin Cai,[a] Xin Wen,[a] Jingwei Cui,[b] Xiuqi Jin,[b] Huiling Wang,[b] Wei Li*[b] and Hongbing Deng*[a, b]

a. Innovation Center for Textile Science and Technology, Donghua University, Shanghai, 200051 China. E-mail: hbdeng@whu.edu.cn.

b. Hubei Key Laboratory of Biomass Resource Chemistry and Environmental Biotechnology, Hubei Engineering Center of Natural Polymers-based Medical Materials, School of Resource and Environmental Science, Wuhan University, Wuhan, 430079 China. E-mail: liwei418@whu.edu.cn.

Material preparation

Preparation of TiO_2 NF

First, 0.5 g of polyvinylpyrrolidone (PVP, Mw = 1,300,000) was added to a mixed solution of 8 g of ethanol and 4 g of acetic acid and dissolved under vigorous stirring for 4 h. Subsequently, 4.2 g of titanium (IV) isopropoxide and 0.9 g of zirconium acetate were slowly added dropwise to the above solution and stirred in an ice-water for 30 min to obtain a precursor solution. The precursor solution was then transferred into a syringe and pumped at a fixed speed of 0.6 mL h^{-1}. A voltage of 18 kV and a tip-to-collector distance of 15 cm were applied to generate stable jet flows. During the preparation, the temperature and relative humidity were maintained at 25 ± 2 °C and 45 ± 2%, respectively. The precursor nanofibers were collected on a roller covered with nonwoven fabric and then dried in a vacuum oven at 60 °C for 12 h. Finally, the obtained precursor nanofibers were annealed in air at 600 °C for 1 h with a heating rate of 2 °C min^{-1} to obtain titanium dioxide nanofibers. The introduction of zirconium (via zirconium acetate) into the electrospinning precursor inhibited excessive growth of TiO_2 grains during annealing, reduced the brittleness associated with high crystallinity, and endowed the nanofibers with excellent flexibility, allowing the fibers to maintain their intact fibrous structure without collapse after annealing at 600 °C.

Preparation of Cu_1-Co_1/TiO_2

The TiO_2 nanofibers were heated to 500°C at a heating rate of 5°C/min under a 5% H_2/Ar flow and annealed at this temperature for 3 hours. This treatment introduces oxygen vacancies into the TiO_2 lattice, resulting in TiO_{2-x} ($0 < x < 2$). Additionally, TiO_{2-x} samples with different oxygen vacancy concentrations were prepared by varying the annealing time to 2 hours and 4 hours. To fabricate atomically dispersed catalysts on TiO_2, the oxygen-deficient TiO_{2-x} was immersed in a mixed solution of 3 M $CuCl_2$ and 3 M $Co(NO_3)_2$ under magnetic stirring for 48 hours. This allows sufficient infiltration of Cu^{2+} and Co^{2+} ions into the oxygen vacancies. The precipitate was then collected by suction filtration, washed alternately several times with ultrapure water and ethanol to remove weakly adsorbed or unreacted ions, and dried under vacuum at 60°C for 12 hours. Finally, the dried precipitate was further heated to 500°C at a heating rate of 5°C/min under a 5% H_2/Ar flow and annealed again for 3 hours. During this process, Cu^{2+} and Cu^{2+} are reduced to Cu and Co atoms, respectively, forming strong bonds with the TiO_2 surface and anchoring at the oxygen vacancy sites, thereby yielding Cu_1–Co_1/TiO_2 with isolated Cu and Co atoms dispersed on the TiO_2 support.

Preparation of Cu_1/TiO_2、Co_1/TiO_2 and Cu_1-Co_1/TiO_2 NP

The preparation methods for Cu_1/TiO_2 and Co_1/TiO_2 are the same as that for Cu_1–Co_1/TiO_2, with the only difference being that during single-atom doping, the TiO_{2-x} ($0 < x < 2$) containing oxygen vacancies is immersed in 3 M copper chloride ($CuCl_2$) and 3 M cobalt nitrate ($Co(NO_3)_2$) solutions, respectively. For Cu_1–Co_1/TiO_2 nanoparticles (NPs), the precursor solution of TiO_2 was not electrospun into fibrous morphology; instead, the precursor solution was directly dried, ground into powder, and then annealed. The annealing conditions and subsequent experimental steps are the same as those for Cu_1–Co_1/TiO_2.

Materials characterizations

The surface morphology of the catalyst was observed by ZEISS GeminiSEM 300 field emission scanning electron microscope (SEM), Thermo Fisher Titan Themis G2 60-300 high angle annular dark field scanning transmission electron microscopy (HAADF-STEM), and JEOL JEM 2100F for High-resolution transmission electron microscopy (HRTEM). Phase analysis was obtained by Rigaku Miniflex 600 X-ray diffractometer (XRD). Valence state of the catalyst was analyzed by using Thermo Scientific K-Alpha X ray photoelectron spectroscope (XPS) with monochromatic Al Kα as the excitation source, and the binding energies were corrected through C 1s peak (284.8 eV). The ultraviolet-visible absorbance spectra (UV-Vis) used for the detection of N-containing substances and was measured by UV-2600 spectrophotometer (Shimadzu; Kyoto; Japan). ^{1}H nuclear magnetic resonance (NMR) was performed on AVANCE III 400 MHz (Bruker). Electron paramagnetic resonance (EPR) measurements were performed on a Bruker A300 EPR spectrometer. The online differential electrochemical mass spectrometry (DEMS) was used to detect the intermediates by the QAS 100 (Linglu Instruments (Shanghai) Co. Ltd.). In situ FTIR spectroelectrochemistry measurements were performed on VERTEX 80V spectrometer (Bruker) equipped with a germanium selenide crystal substrate. In situ Raman spectroelectrochemistry experiments were conducted using a microscopic laser confocal Raman spectrometer (inVia, Renishaw) equipped with a 785 nm excitation laser.

Electrochemical measurements

The electrochemical measurements were conducted on a CHI-760E electrochemical workstation using a custom-designed H-cell, with its two compartments separated by a Nafion 117 membrane. The H-cell was equipped with an Ag/AgCl reference electrode and a graphite rod counter electrode. The working electrode was prepared as follows: The catalyst (5 mg) was mixed with 450 μL of ultrapure water, 450 μL of ethanol, and 50 μL of a perfluorosulfonic acid resin solution (Nafion). The resulting mixture was ultrasonicated for 40 minutes to obtain a catalyst ink for the working electrode. Subsequently, 100 μL of the ink was drop-cast onto a pre-treated carbon paper with a working area of 1 × 1 cm². The actual catalyst loading was 0.5 mg cm^{-2}. The working electrolyte for NO_3RR consisted of 0.5 M K_2SO_4 and 0.5 M KNO_3. Before the reaction, Ar gas (99.999%) was purged into the electrolyte for 30 minutes to completely remove dissolved O_2. Linear sweep voltammetry (LSV) was performed at a scan rate of 5 mV s^{-1} with 90% iR compensation. Chronoamperometry tests were carried out in the potential range from –0.6 V to –0.9 V vs. RHE, with a duration of 30 minutes at each potential and a stirring rate of 500 rpm. After the i-t tests at selected potentials, the produced NH_3 was analyzed by UV-Vis spectroscopy and ^{1}H nuclear magnetic resonance (NMR). All electrochemical data are averaged from at least three independent parallel experiments, with standard deviations calculated as bars of error. All potentials reported in this work were calibrated to the reversible hydrogen electrode (RHE) scale using the equation: $E_{RHE}=E_{Ag/AgCl}+0.197+0.0591\times pH$

Determination of NH_3

UV-vis spectroscopy method

First, a 100 ppm NH_4^+ standard solution was diluted to prepare a series of standard solutions with appropriate ammonium ion concentrations. Then, 2 mL of each prepared standard solution was taken, and 2 mL of color reagent A (1 M NaOH solution containing 5 wt% sodium citrate and 5 wt% salicylic acid), 1 mL of color reagent B (0.05 M NaClO solution), and 200 μL of color reagent C (1 wt% sodium nitroferricyanide solution) were added sequentially. After incubation for 2 hours at room temperature under light-proof conditions, the UV–vis

absorbance of the mixed solution was measured at a wavelength of 655 nm. A standard curve was plotted with absorbance versus ammonium ion concentration. After the chronoamperometry test, the concentration of NH_4^+ in the catholyte was determined similarly: the electrolyte was appropriately diluted, the color reagents were added stepwise, and the UV-vis absorbance was measured. The NH_4^+concentration was then determined by comparison with the standard curve. All measurements were repeated at least three times.

^{1}H nuclear magnetic resonance (NMR) Method

For comparison with the UV-vis spectroscopy method, the concentration of NH_4^+in the solution after the nitrate reduction reaction was quantitatively determined using a 600 MHz proton nuclear magnetic resonance (^{1}H NMR) spectrometer. After electroreduction, the electrolyte was collected and quantified via ^{1}H NMR (600 MHz) using maleic acid as an internal standard. The calibration curve was established as follows: First, a series of standard NH_4^+–N solutions with known concentrations (20, 30, 40, 50, and 60 ppm) were prepared in 0.05 M H_2SO_4. Second, 20 μL of each standard NH_4^+–N solution at different concentrations was mixed with 4 mg of maleic acid. Third, 50 μL of deuterium oxide (D_2O) was added to 0.5 mL of the mixed solution for NMR detection. Fourth, calibration was performed based on the peak area ratio between NH_4^+-N and maleic acid, as the NH_4^+-N concentration showed a positive correlation with the area ratio.

Determination of Nitrite (NO_2^-)

First, 20 g of sulfanilamide and 1 g of N-(1-naphthyl) ethylenediamine dihydrochloride were accurately weighed and added to a mixture of 50 mL of phosphoric acid and 500 mL of ultrapure water. The solution was stirred thoroughly until complete dissolution of the solids and then homogenized to obtain the nitrite chromogenic solution. Next, a series of NO_2^--N standard solutions at different concentrations were prepared. Exactly 5 mL of each standard solution was pipetted, mixed with 100 μL of the above chromogenic working solution, and allowed to react at room temperature in the dark for 20 min. After the reaction, the absorbance was measured at 540 nm using a UV-vis spectrophotometer. A standard curve was plotted with the NO_2^--N concentration as the abscissa and the absorbance as the ordinate. Following the chronoamperometry test, the electrolyte from the cathode compartment was appropriately diluted and processed according to the above coloring procedure for measurement. The concentration of NO_2^--N in the electrolyte was calculated from the measured absorbance values based on the standard curve.

Calculation of Faradaic Efficiency (FE) and Yield Rate

The Faradaic efficiency (FE) and yield rate were calculated using the following equations:

$$FE(NH_3) = \frac{8 \times F \times c_{NH_3} \times V}{Q}$$

$$FE(NO_2^-) = \frac{2 \times F \times c_{NO_2^-} \times V}{Q}$$

$$Yield(NH_3) = \frac{c_{NH_3} \times V}{M_{NH_3} \times t \times S}$$

$$Yield(NO_2^-) = \frac{c_{NO_2^-} \times V}{M_{NO_2^-} \times t \times S}$$

where the parameters are defined as follows:

c: the measured concentration of the product (NH_3 or NO_2^-) in the catholyte;

F: the Faraday constant (96485 C mol^{-1});

V: the volume of the electrolyte (35 mL in this experiment);

Q: the total charge passed during the chronoamperometry test;

t: the electrolysis time;

S: the geometric surface area of the electrode (1 cm^2 in this experiment).

Electron Paramagnetic Resonance (EPR) Measurements

Electron paramagnetic resonance (EPR) measurements in this study were performed on a Bruker A300 EPR spectrometer. The central magnetic field was set at 3500 G with a sweep width of 200 G, a sweep time of 30 s, a microwave power of 19.45 mW, a modulation amplitude of 1 G, a conversion time of 40 ms, and a frequency of 9.852508 GHz. The specific procedure was as follows: First, 5,5-dimethyl-1-pyrroline N-oxide (DMPO) was diluted with ultrapure water at a volume ratio of 1:20. Then, electrolysis was conducted at -1.5 V (vs. RHE) for 10 min in electrolytes without NO_3^- and with NO_3^-, respectively. After electrolysis, 100 μL of the diluted DMPO solution was added to the electrolyte. Subsequently, 1 mL of the solution was immediately sampled for EPR testing. The tests were carried out using a CHI 760 electrochemical workstation, with a saturated Ag/AgCl electrode and a graphite rod serving as the reference and counter electrodes, respectively.

The Online DEMS measurement

Online DEMS measurements were conducted using a QAS 100 instrument (Linglu Instruments, Shanghai). An Au-coated gas-permeable membrane loaded with the catalyst, a saturated Ag/AgCl electrode, and a graphite rod were used as the working electrode, reference electrode, and counter electrode, respectively. Before and after the DEMS measurements, Ar was continuously bubbled into the electrolyte containing 0.5 M K_2SO_4 and 0.5 M KNO_3. CV was performed in the range of 0 to −1.4 V vs. RHE at a scan rate of 50 $mV \cdot s^{-1}$ for 6 cycles.

In situ FTIR spectroelectrochemistry

In situ FTIR spectroelectrochemistry measurements were performed on VERTEX 80V spectrometer (Bruker) equipped with a germanium selenide crystal substrate. The measurements were performed using a CHI 760 electrochemical workstation. The detailed procedure was as follows: First, the working electrode was prepared by securing carbon paper, which had been drop-casted with the catalyst, onto a polished silicon wafer coated with a gold film. A saturated Ag/AgCl electrode and a graphite rod were employed as the reference electrode and counter electrode, respectively. Data acquisition was synchronously carried out during the potential sweep from the open circuit potential to -1.5 V vs. RHE.

In situ Raman spectroelectrochemistry

In situ Raman spectroelectrochemistry experiments were conducted using a microscopic laser confocal Raman spectrometer (inVia, Renishaw) equipped with a 785 nm excitation laser.The tests were conducted using a CHI 760 electrochemical workstation within a customized spectroelectrochemical cell, employing a graphite rod as the counter electrode and a saturated Ag/AgCl electrode as the reference electrode. The electrolyte used was a 0.5 M K_2SO_4 solution saturated with Ar. Operando Raman spectra were obtained via chronoamperometry at room temperature, with data acquisition performed synchronously during the potential sweep from the open circuit potential to -1.5 V vs. RHE.

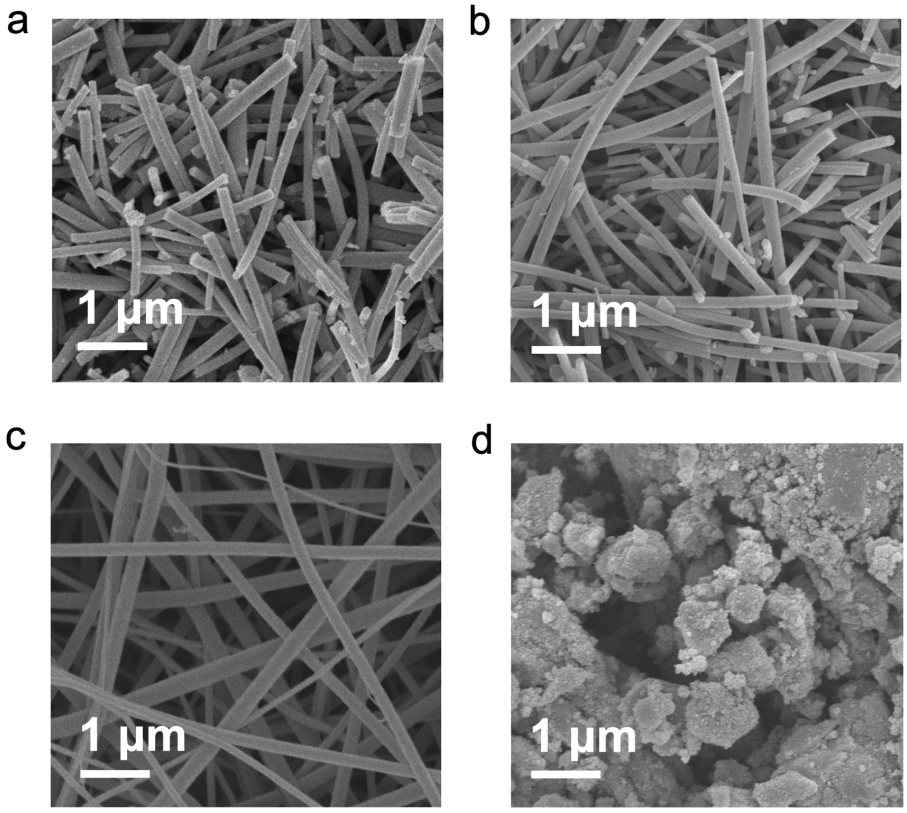

Fig. S1 SEM of (a) Cu_1/TiO_2, (b) Co_1/TiO_2, (c) TiO_2 and (d) Cu_1-Co_1/TiO_2 NP

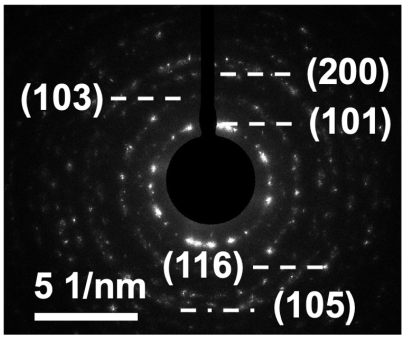

Fig. S2 SAED pattern of Cu_1-Co_1/TiO_2

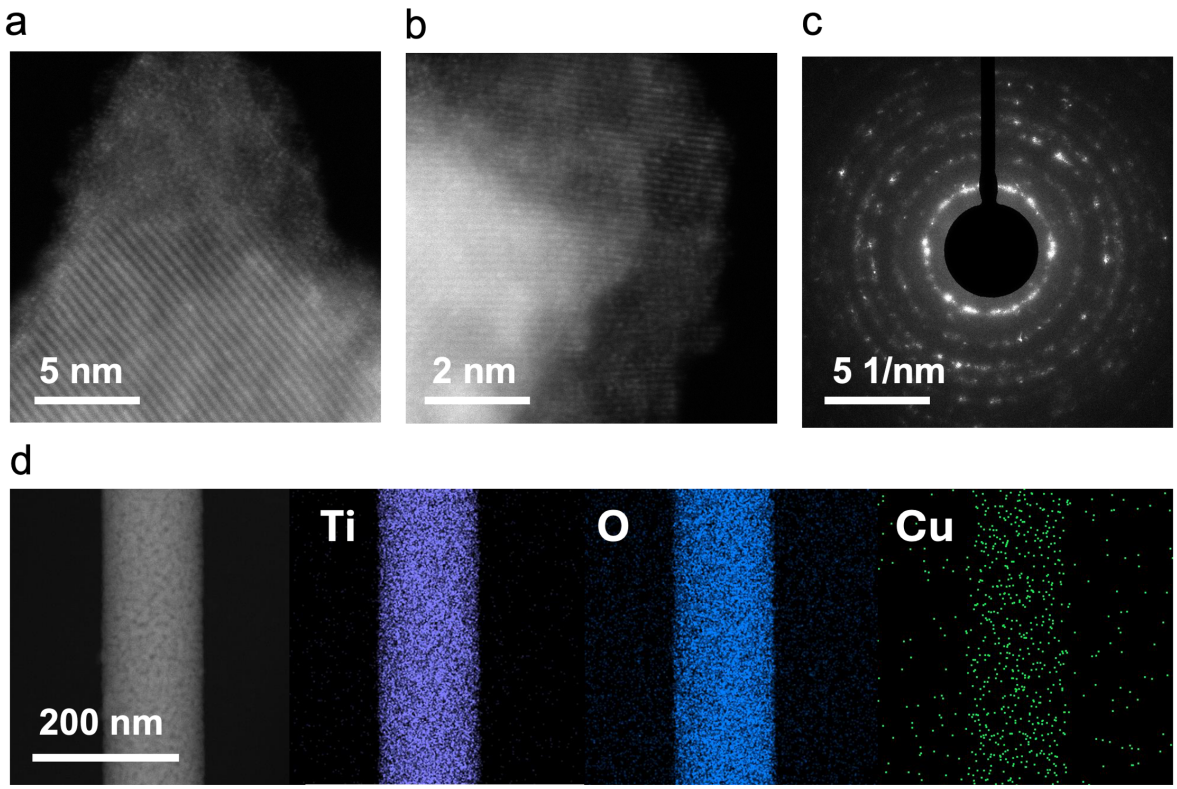

Fig. S3 (a) HRTEM image, (b) HAADF-STEM image, (c) SAED pattern and (d) TEM image and the EDS mapping images of Cu_1/TiO_2.

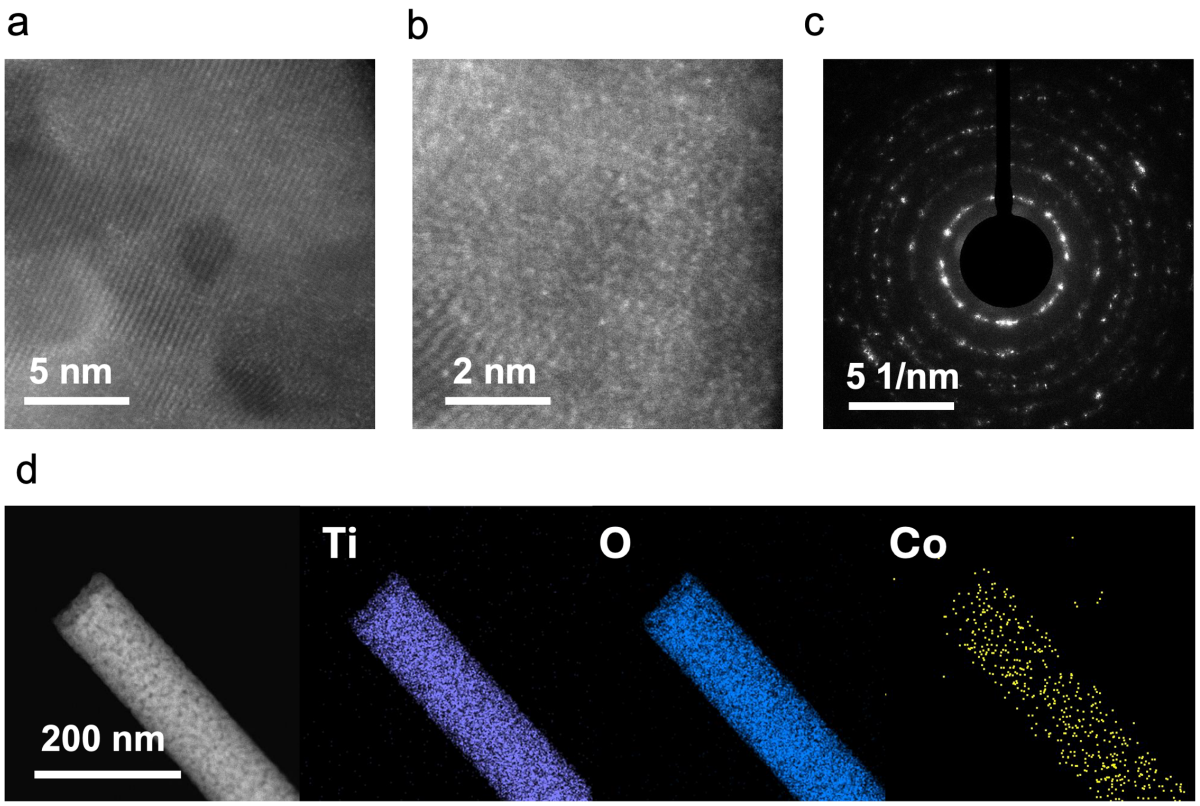

Fig. S4 (a) HRTEM image, (b) HAADF-STEM image, (c) SAED pattern and (d) TEM image and the EDS mapping images of Co_1/TiO_2.

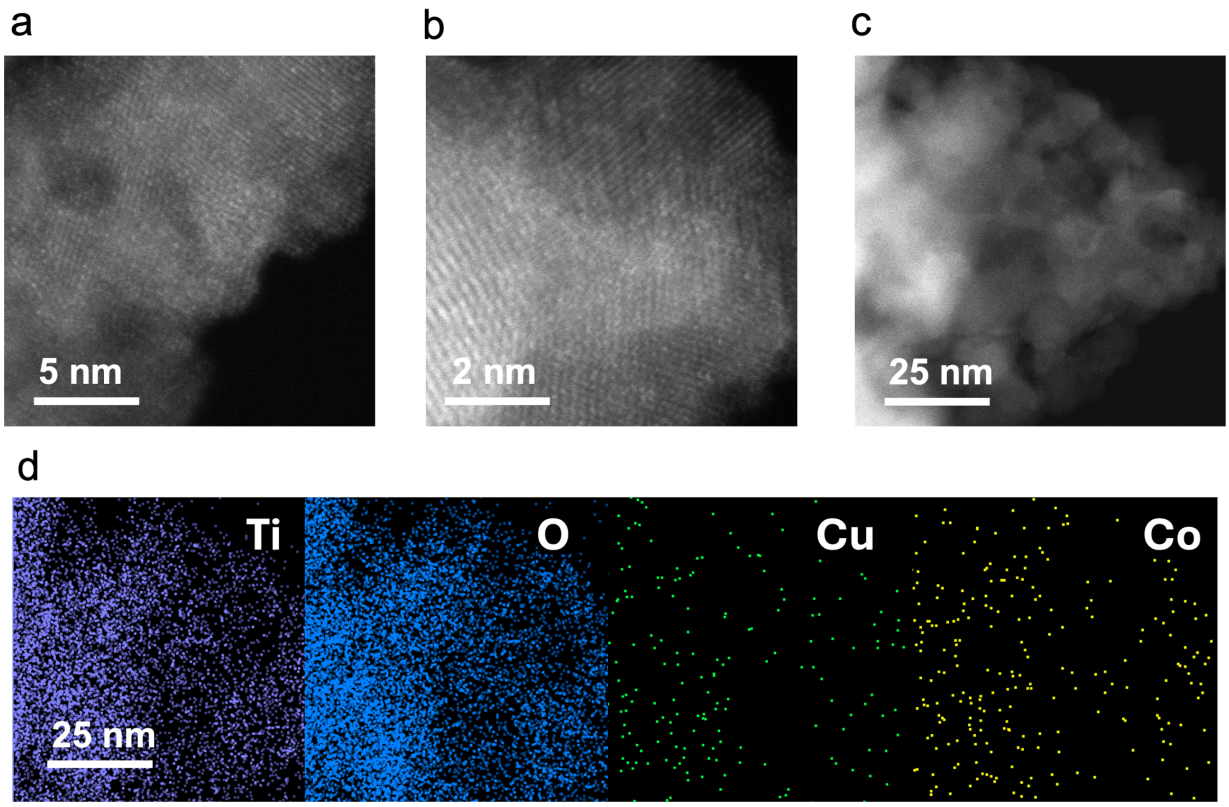

Fig. S5 (a) HRTEM image, (b) HAADF-STEM image, (c) SAED pattern and (d) TEM image and the EDS mapping images of Cu_1-Co_1/TiO_2 NP.

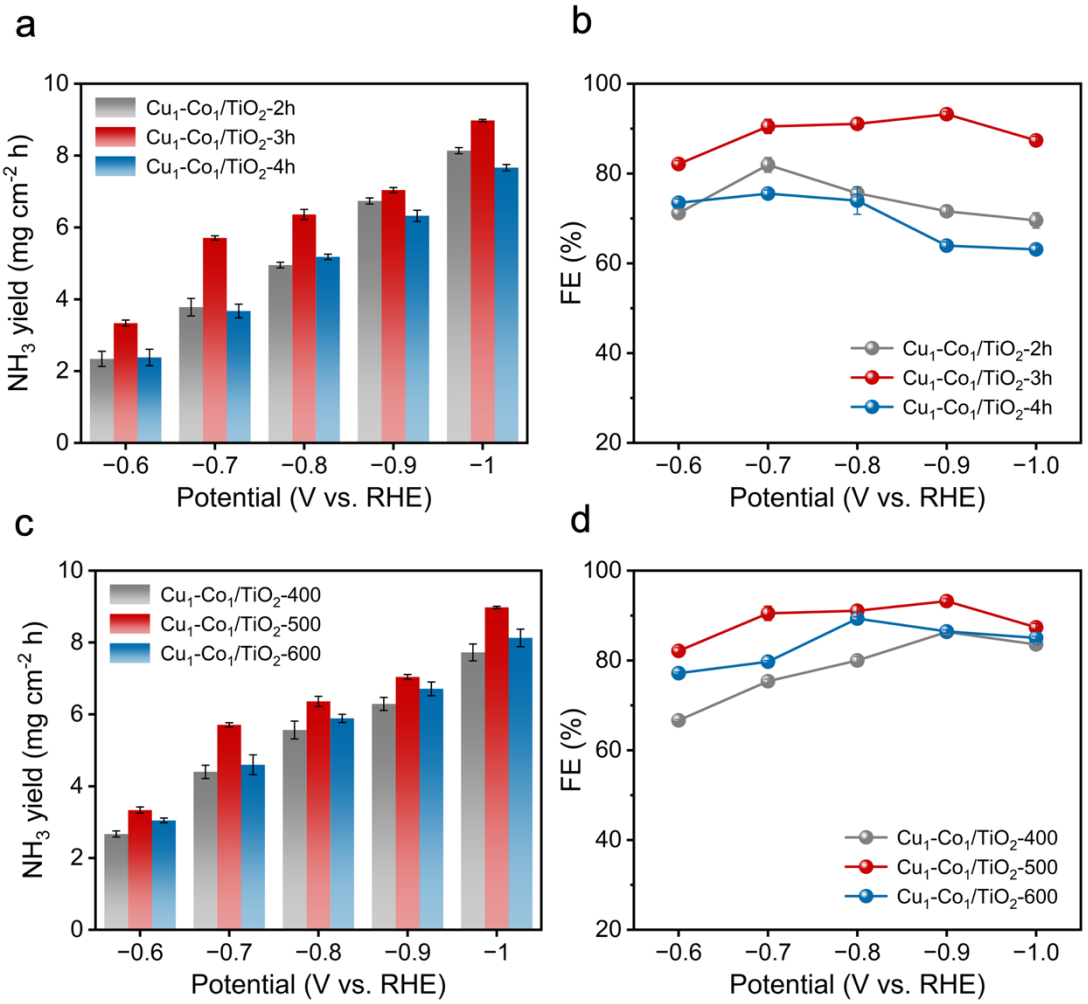

Fig. S6 (a) NH_3 yield and (b) FE of Cu_1-Co_1/TiO_2 catalyst at different annealing times in 0.5 M K_2SO_4 with 0.5 M KNO_3. (c) NH_3 yield and (d) FE of Cu_1-Co_1/TiO_2 catalyst at different annealing temperatures in 0.5 M K_2SO_4 with 0.5 M KNO_3.

The results show that within the potential range of –0.7 to –0.9 V vs. RHE, the sample annealed at 500 °C for 3 h exhibits the optimal NH_3 yield and FE > 90%. A suitable concentration of oxygen vacancies (3 h/500 °C) can not only stably anchor Cu and Co single atoms, maintaining high dispersion and providing sufficient active sites, but also modulate the electronic structure through strong interactions between single atoms and oxygen vacancies, effectively suppressing the HER, thereby achieving both high activity and high selectivity.

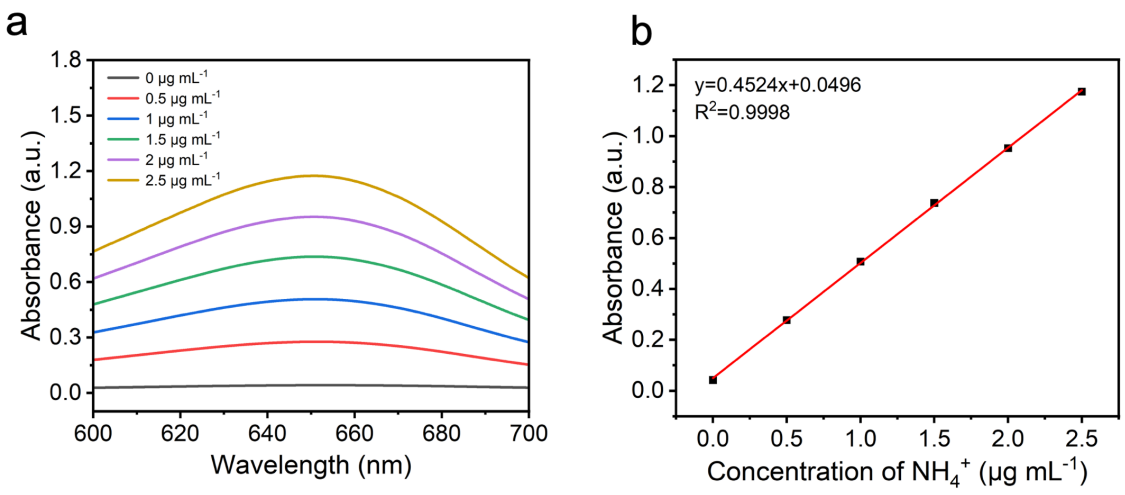

Fig. S7 (a) UV–vis absorption spectra of electrolyte with different concentration of NH_4^+. (b) The corresponding calibration curve for NH_4^+ quantification.

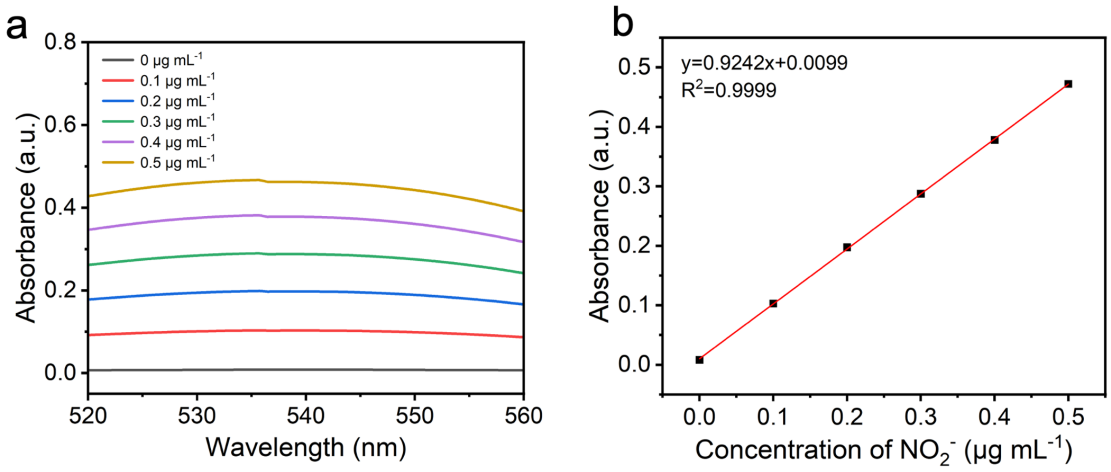

Fig. S8 (a) UV–vis absorption spectra of electrolyte with different concentration of NO_2^-. (b) The corresponding calibration curve for NO_2^- quantification.

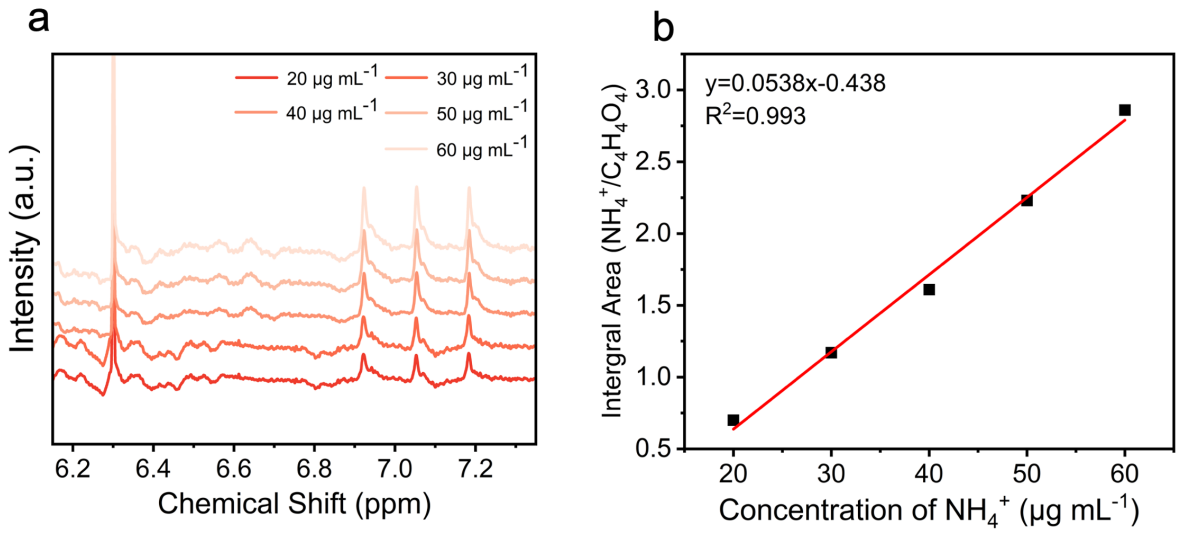

Fig. S9 (a) ^{1}H-NMR spectra of NH_4^+ at different concentrations. (b) The standard curve of the integral area ($NH_4^+/C_4H_4O_4$) against the NH_4^+ concentration.

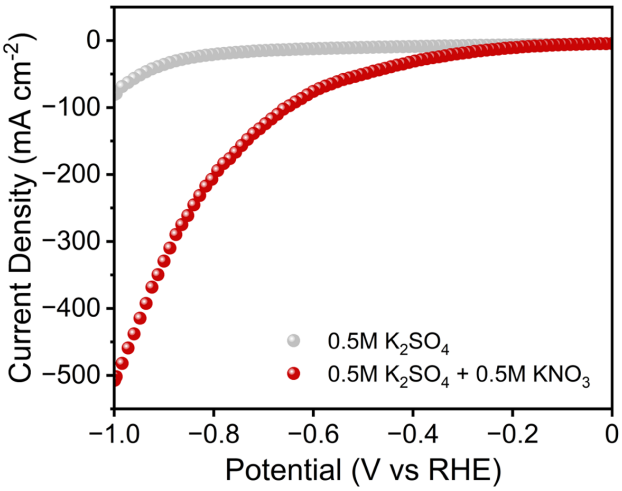

Fig. S10 The LSV curves for Cu_1-Co_1/TiO_2 in 0.5 M K_2SO_4 with or without 0.5 M KNO_3.

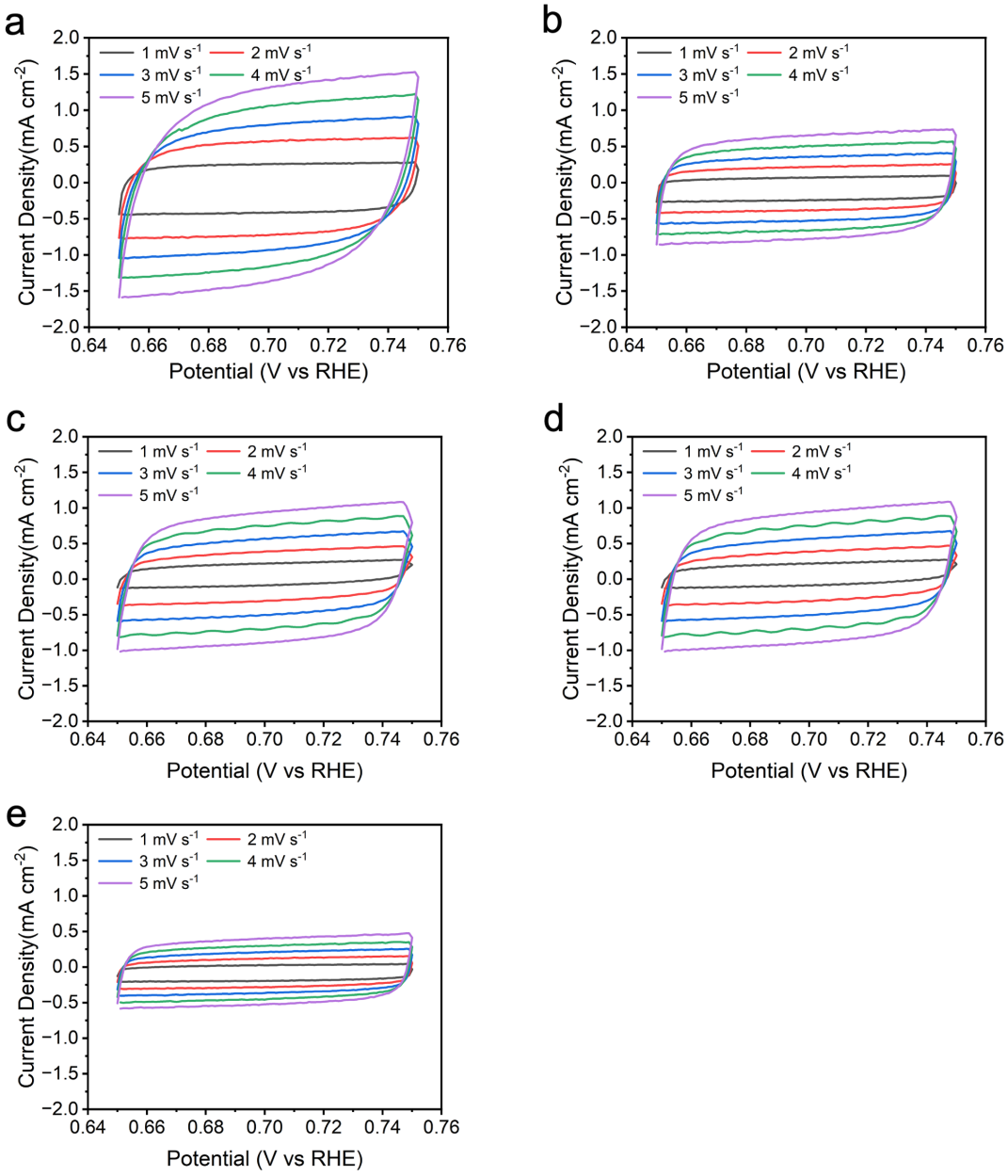

Fig. S11 Cyclic voltammograms (CV) profiles obtained on the (a) Cu_1-Co_1/TiO_2, (b) Cu_1/TiO_2, (c) Co_1/TiO_2, (d) Cu_1-Co_1/TiO_2 NP and (e) TiO_2.

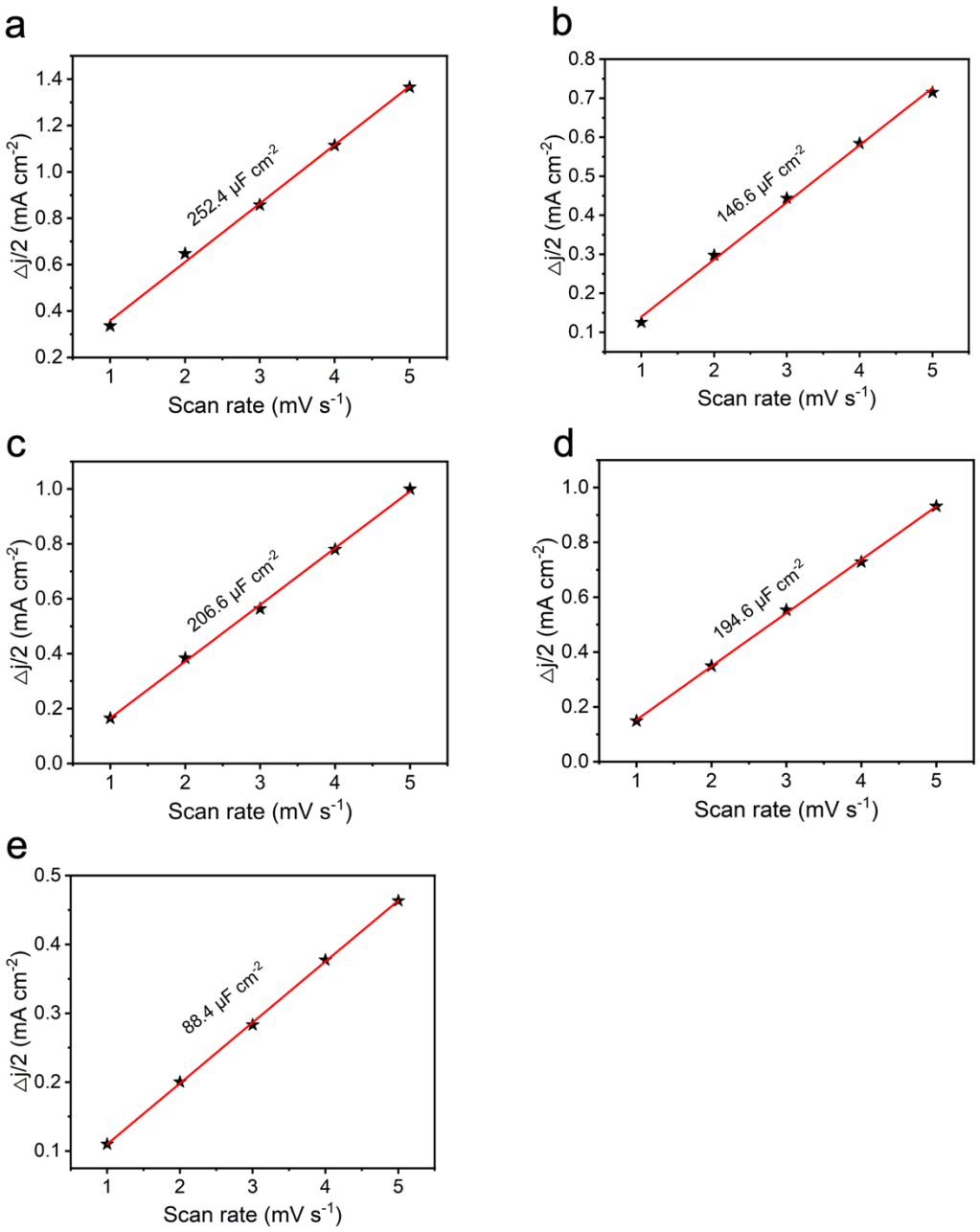

Fig. S12 The determination of double layer capacitance (C_{dl}) for (a) Cu_1-Co_1/TiO_2, (b) Cu_1/TiO_2, (c) Co_1/TiO_2, (d) Cu_1-Co_1/TiO_2 NP and (e) TiO_2.

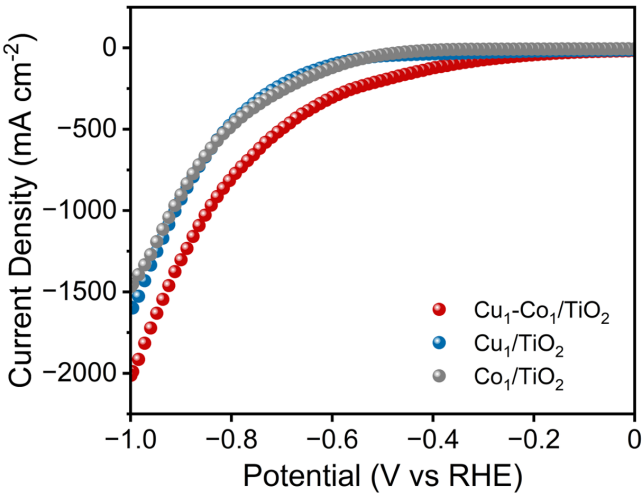

Fig. S13 Double layer capacitance normalized LSV curves of Cu_1/TiO_2, Co_1/TiO_2 and Cu_1-Co_1/TiO_2.

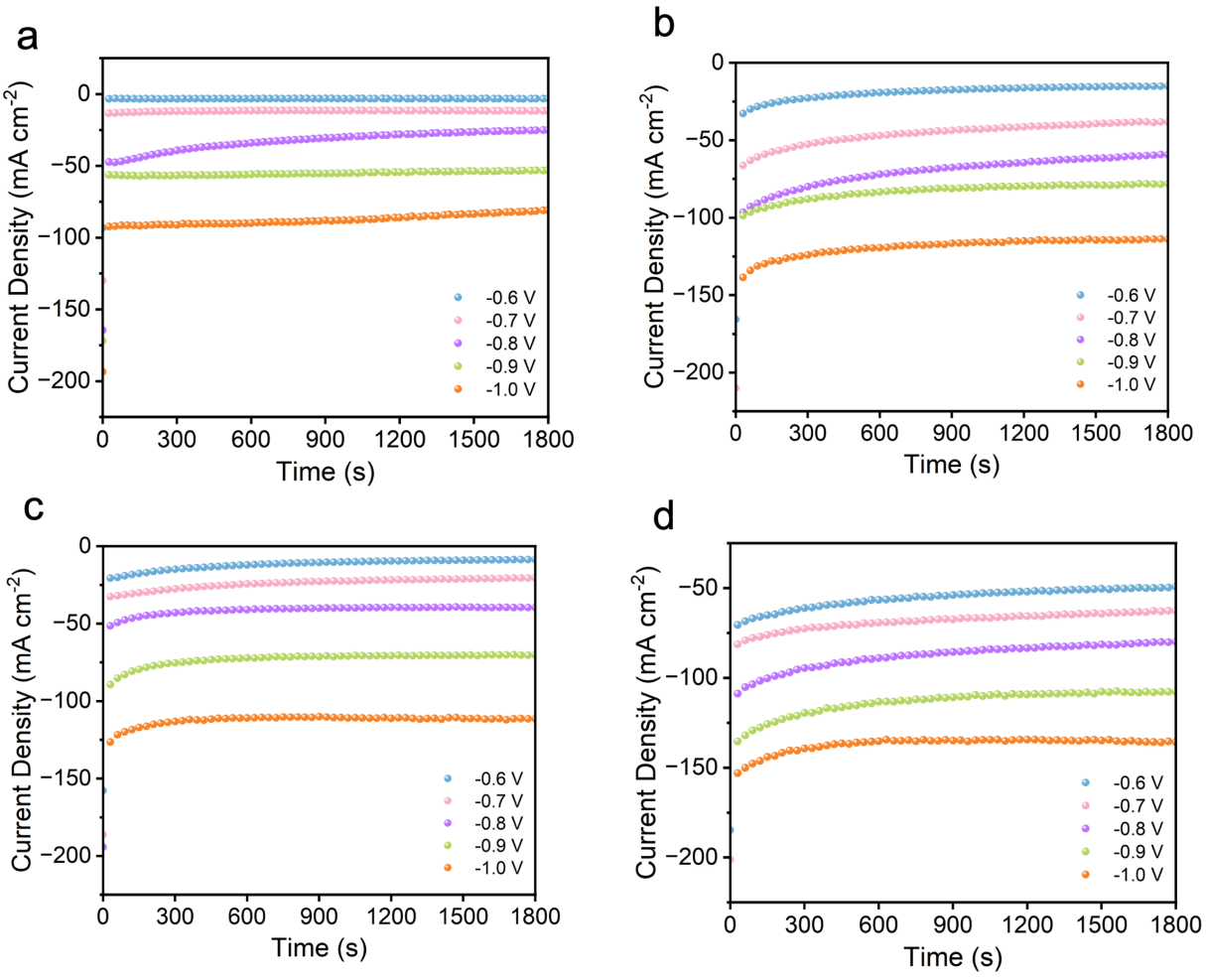

Fig. S14 The chronoamperometric curves performed at various applied potentials over (a) TiO_2, (b) Cu_1/TiO_2, (c) Cu_1/TiO_2 and (d) Cu_1-Co_1/TiO_2.

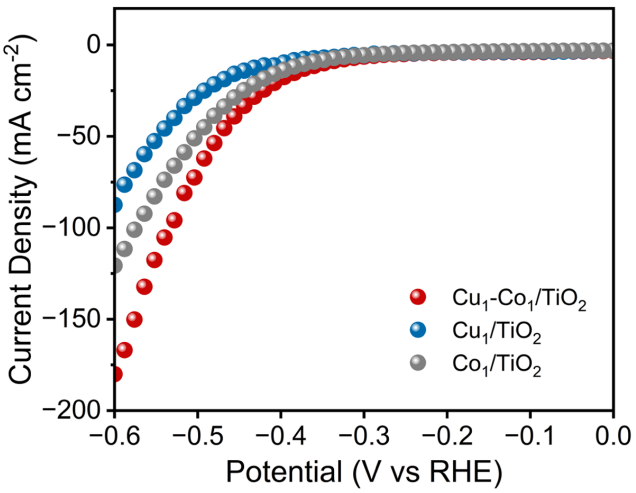

Fig. S15 The LSV curves for Cu_1/TiO_2, Co_1/TiO_2 and Cu_1-Co_1/TiO_2 in 0.5 M K_2SO_4 with 0.5 M KNO_2.

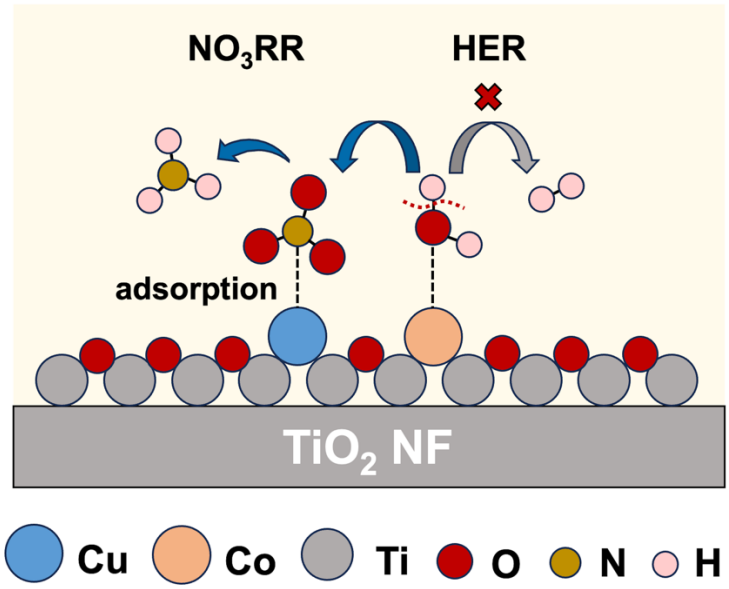

Fig. S16 Schematic diagram of atomic scale adsorbed hydrogen relay transfer.

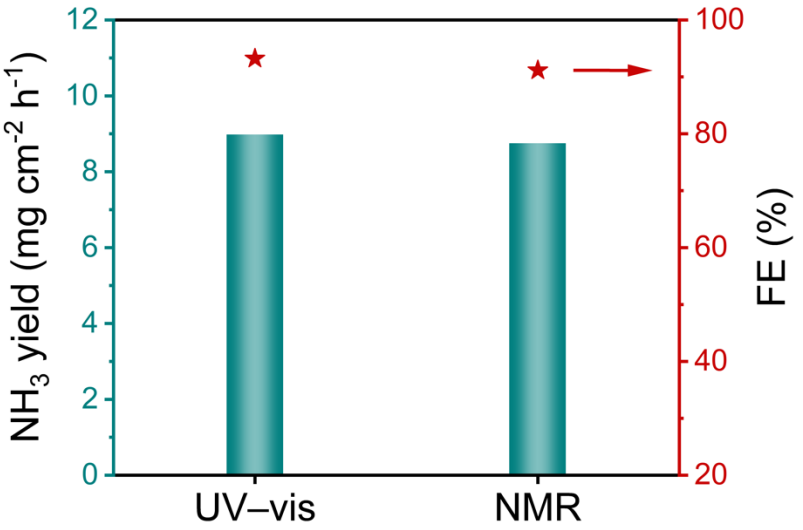

Fig. S17 NH_3 yield rate and FE of Cu_1-Co_1/TiO_2 electrodes at −0.9 V vs RHE by UV–vis absorption spectroscopy and 1 H NMR spectroscopy.

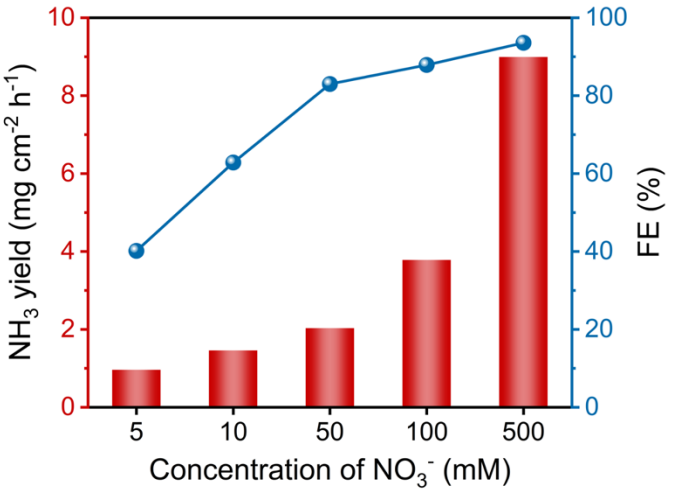

Fig. S18 The NH_3 yield rate and the FE of NH_3 for Cu_1-Co_1/TiO_2 in 0.5 M K_2SO_4 with different concentrations of KNO_3.

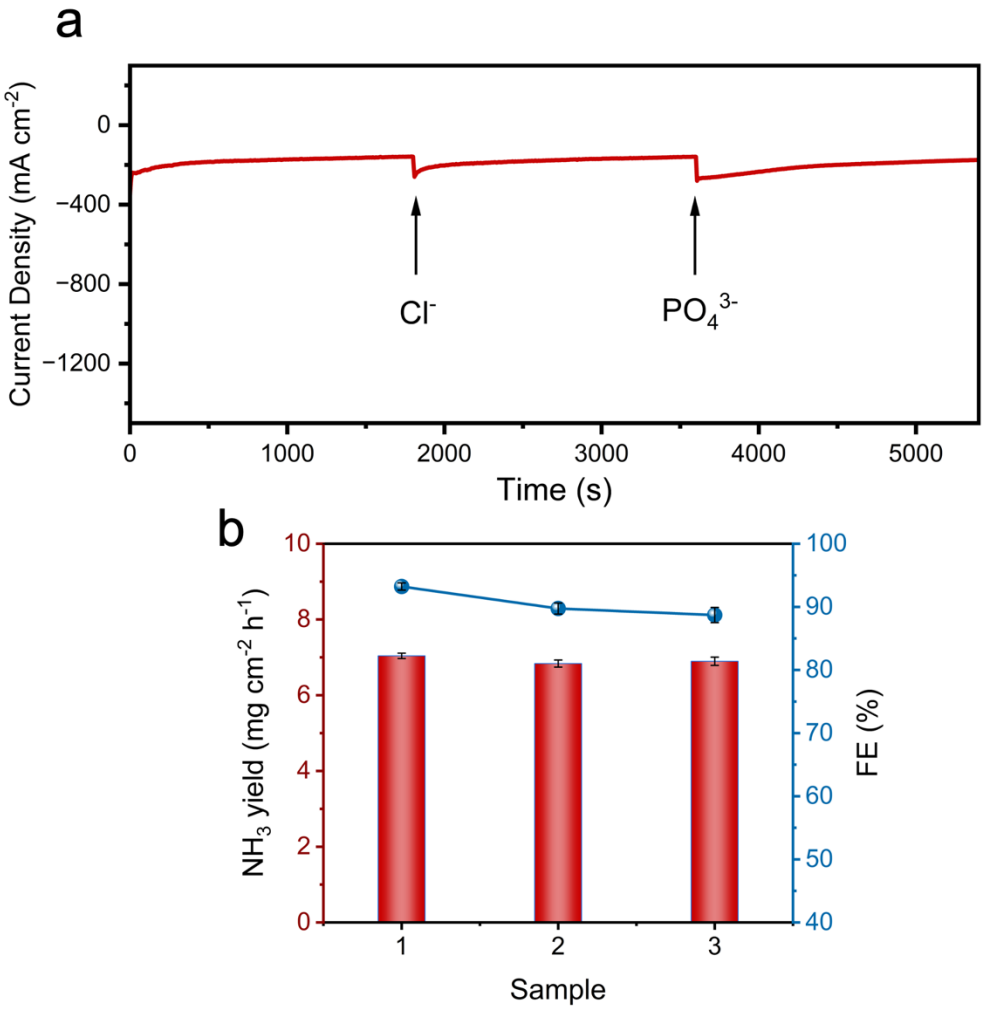

Fig. S19 (a) Chronoamperometric curve of Cu_1-Co_1/TiO_2 after addition of Cl^- and PO_4^{3-}. (b) NH_3 yield and FE of Cu_1-Co_1/TiO_2 after addition of Cl^- and PO_4^{3-} (Sample 1 is the original electrolyte, Sample 2 is the electrolyte after addition of Cl^-, and Sample 3 is the electrolyte after addition and PO_4^{3-})

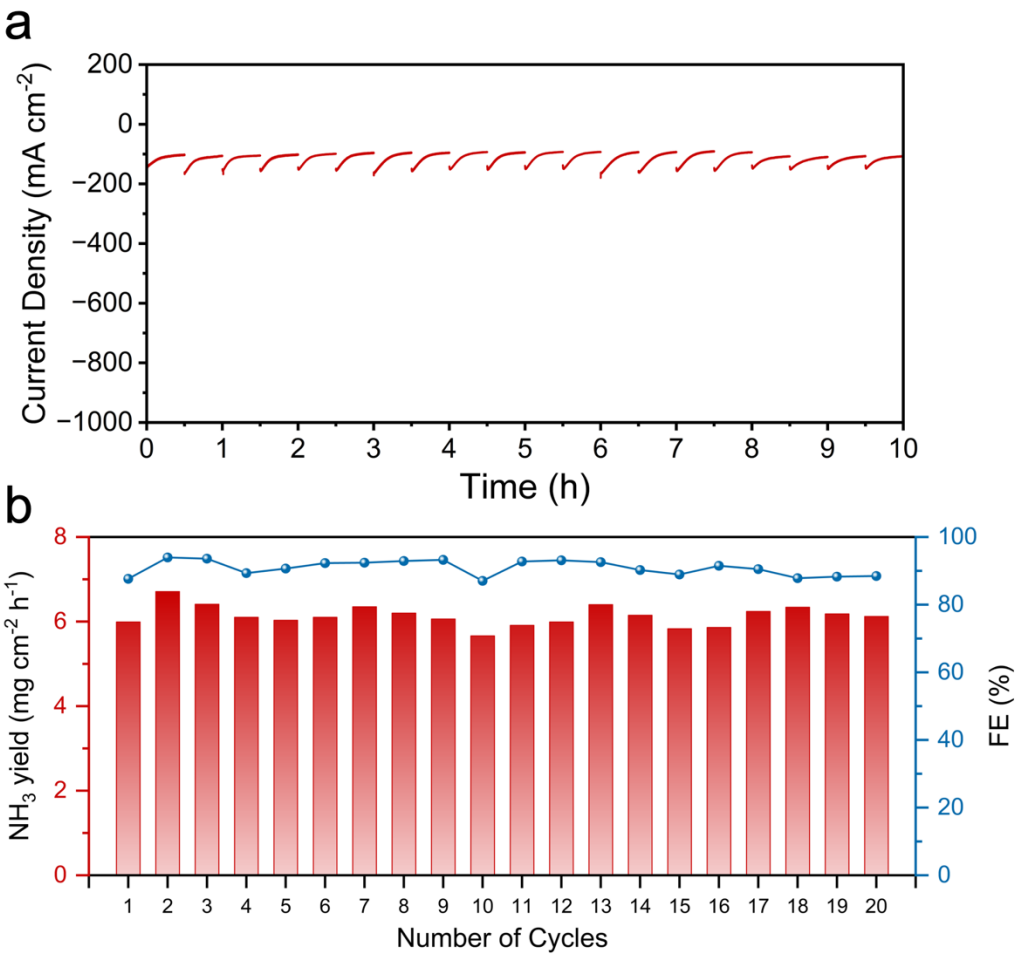

Fig. S20 (a) The chronoamperometric curves for 10 hours of continuous reaction over Cu_1-Co_1/TiO_2 for NO_3RR at −0.9 V vs. RHE. (b) FE and yield rate of NH_3 in 20 consecutive cycles over Cu_1-Co_1/TiO_2 for NO_3RR at −0.9 V vs. RHE.

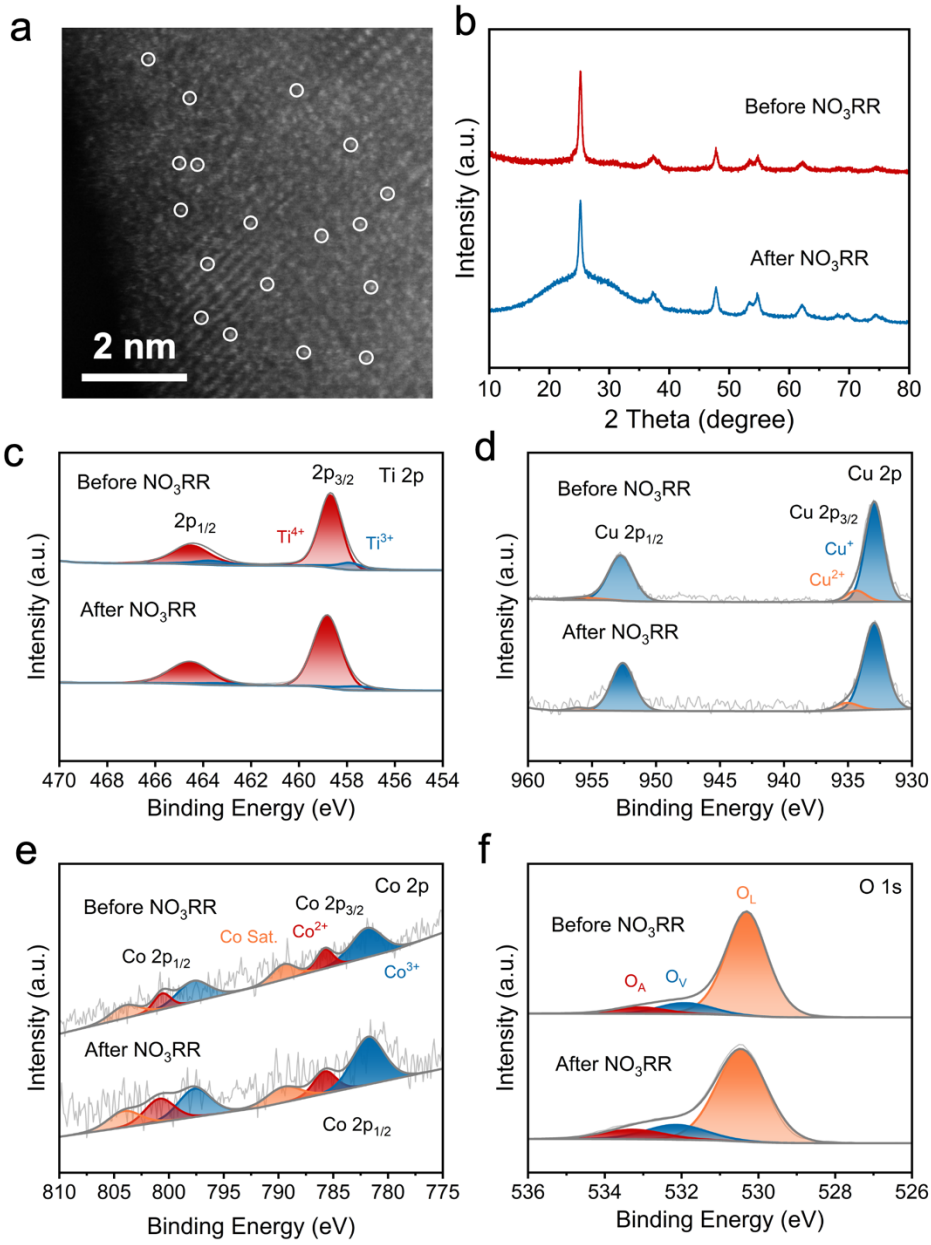

Fig. S21 (a) HAADF-STEM image of Cu_1-Co_1/TiO_2 after NO_3RR. (b) XRD patterns of Cu_1-Co_1/TiO_2 before and after NO_3RR. (c) Ti 2p、(d) Cu 2p、(e) Co 2p and (f) O 1s XPS spectra of Cu_1-Co_1/TiO_2 before and after NO_3RR.

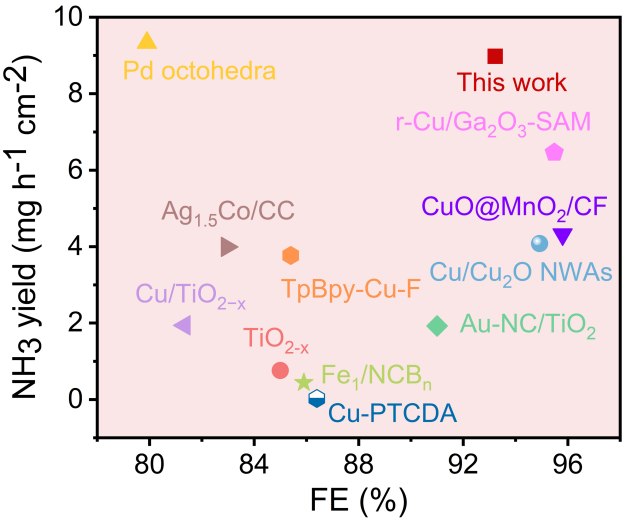

Figure S22 Comparison of FE and NH_3 yield of Cu_1-Co_1/TiO_2 with the reported NO_3RR electrocatalysts

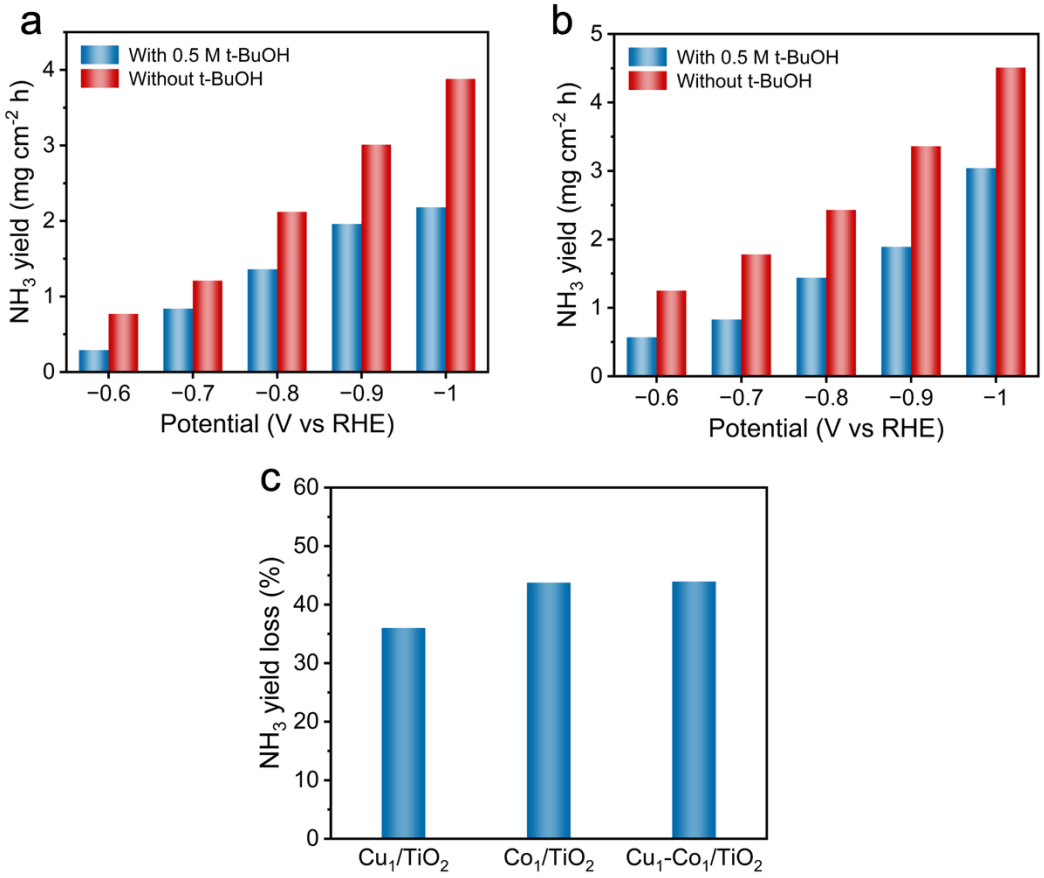

Fig. S23 The NH_3 yield of (a) Cu_1/TiO_2 and (b) Co_1/TiO_2 with and without t-BuOH. (c) The NH_3 yield loss rate of Cu_1/TiO_2, Co_1/TiO_2 and Cu_1-Co_1/TiO_2 after t-BuOH addition in electrolyte.

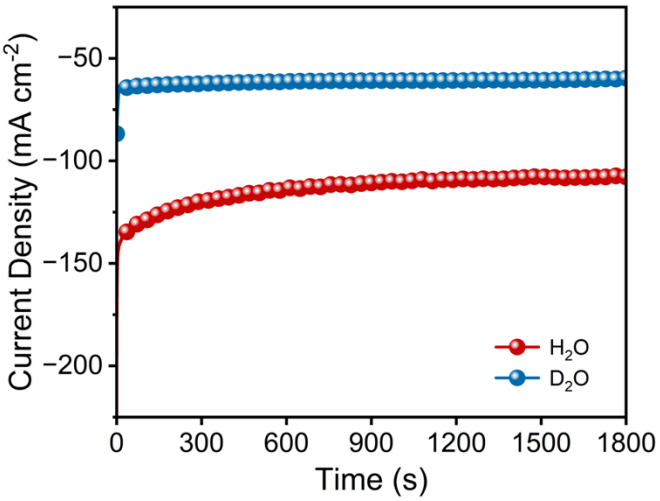

Fig. S24 The chronoamperometric curves with H_2O and D_2O as electrolytes at -0.9 V vs. RHE, respectively.

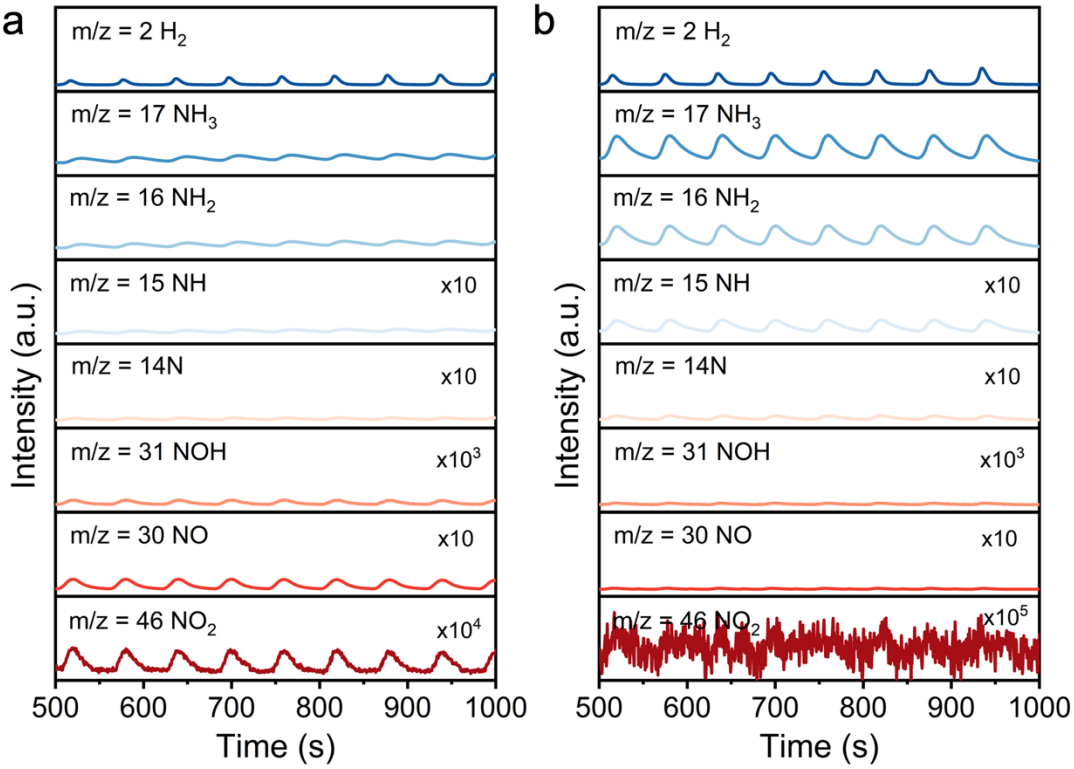

Fig. S25 The electrochemical online DEMS of (a) Cu_1/TiO_2 and (b) Co_1/TiO_2 in 0.5 M K_2SO_4 with 0.5 M KNO_3.

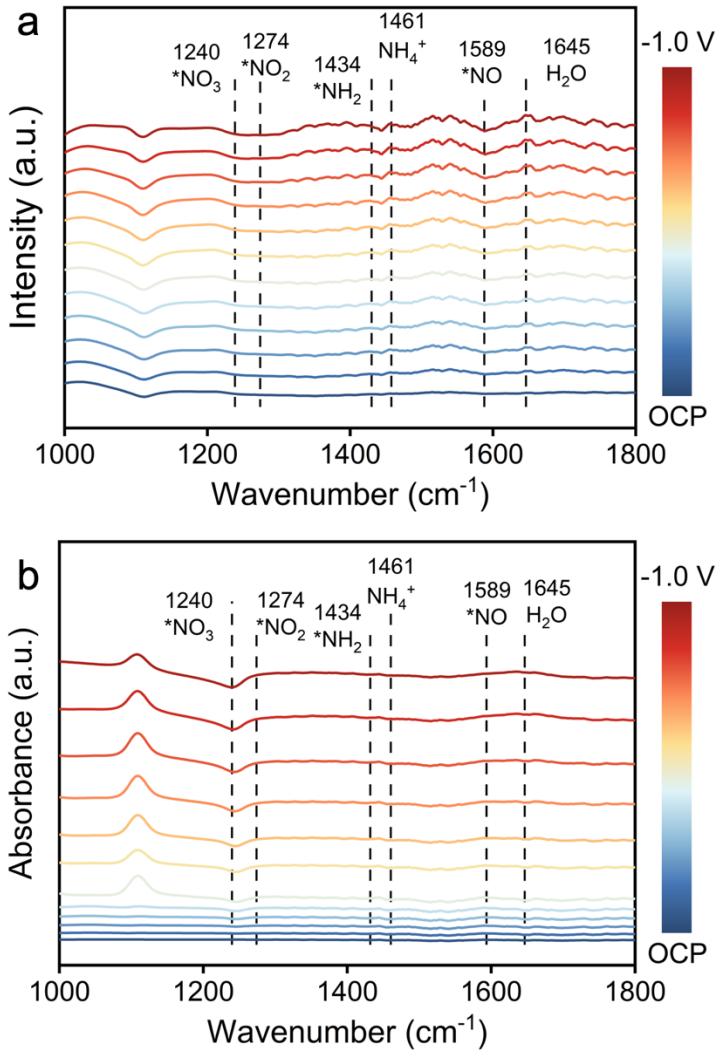

Fig. S26 In situ FTIR of (a) Cu_1/TiO_2 and (b) Co_1/TiO_2 in 0.5 M KNO_3 and 0.5 M K_2SO_4 with different potential.

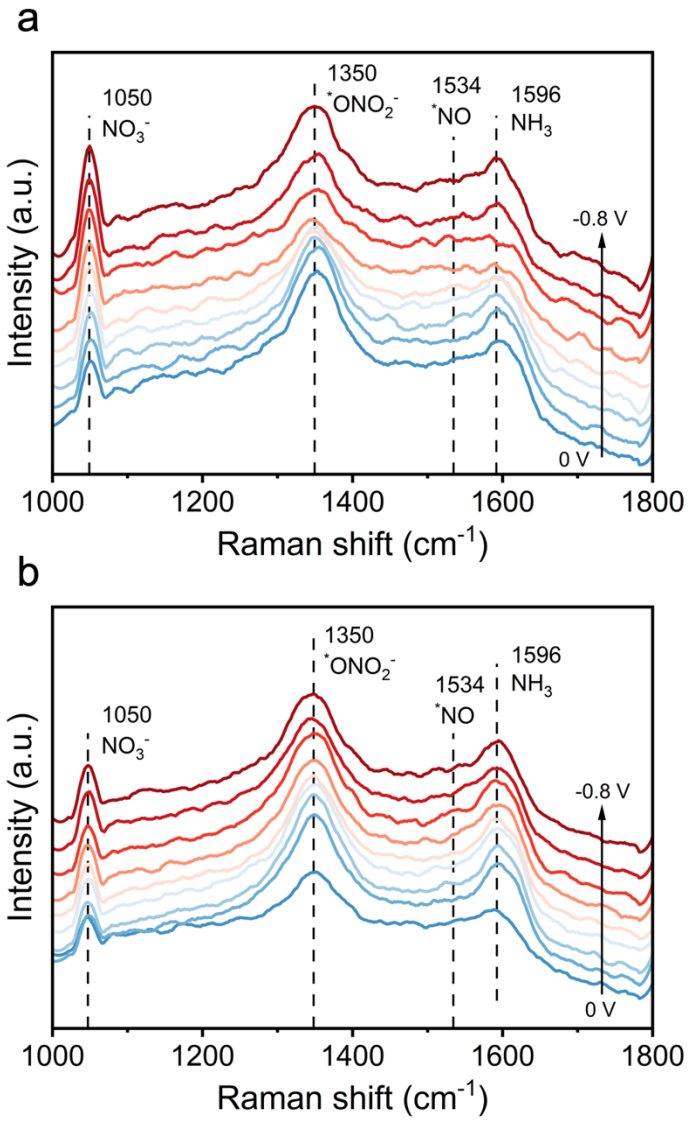

Fig. S27 In situ Raman spectra of (a) Cu_1/TiO_2 and (b) Co_1/TiO_2 in 0.5 M KNO_3 and 0.5 M K_2SO_4 during NO_3RR at different potentials.

Tab. S1 ICP-MS analysis of Cu_1-Co_1/TiO_2, Cu_1/TiO_2, and Co_1/TiO_2

Sample	Cu (wt %)	Co (wt %)
Cu_1-Co_1/TiO_2	0.369	0.39
Cu_1/TiO_2	0.236	/
Co_1/TiO_2	/	0.277

Tab. S2 Fitting results of the EIS on Cu_1-Co_1/TiO_2, Cu_1/TiO_2 and Co_1/TiO_2 obtained from Fig. 3b.

Sample	R_s (Ω)	R_{ct} (Ω)
Cu_1-Co_1/TiO_2	2.831	3.859
Cu_1/TiO_2	2.641	7.952
Co_1/TiO_2	2.21	7.177

Table S3 The electrochemically active surface area (ECSA) of the catalysts.

Sample	**ECSA (cm^{-2})**
Cu_1-Co_1/TiO_2	6.31
Cu_1/TiO_2	3.665
Co_1/TiO_2	5.165

Tab. S4 ICP-MS analysis of Electrolyte after NO_3RR on Cu_1-Co_1/TiO_2.

Element	Content (μg L^{-1})	Leaching Rate (%)
Cu	2.068	3.9
Co	3.580	6.4

Table S5. Comparison of FE and NH_3 yield of Cu_1-Co_1/TiO_2 with the reported NO_3RR electrocatalysts.

Catalysts	Electrolyte	Mass loading (mg cm^{-2})	Electrode type	Potential (V vs. RHE)	FE	NH_3 yield (mg h^{-1} cm^{-2})	Ref.
Cu_1-Co_1/TiO_2	0.5 M K_2SO_4 and 0.5 M KNO_3	0.5	CP	-0.9	93.22	8.98	This work
Co SAs/CNFs	0.1 M KNO_3 and 0.1 M K_2SO_4	0.2	CP	-0.7	91.3	13.43	[1]
TiO_{2-x}	50 ppm NO_3^--N and 0.5M Na_2SO_4	1	CP	-0.97	85	0.76	[2]
Au- NC/TiO_2	0.2 M Na_2SO_4+0.05 M $NaNO_3$	1	CP	-0.6	91	1.923	[3]
Cu/TiO_{2-x}	0.5 M Na_2SO_4 and 200ppm NO_3-N	1	CP	-0.75	81.34	1.94	[4]
TTA-TPH-CuCo	0.5 M K_2SO_4 and 0.1 M KNO_3	0.25	CP	−0.75 V	90.48	14.22	[5]
$Ag_{1.5}Co$/CC	0.5 M K_2SO_4 and 0.1 M KNO_3	0.38	CC	0.75	82.96	3.995	[6]
TpBpy-Cu-F	0.5 M Na_2SO_4+0.1 M $NaNO_3$	1	CP	−0.74	85.4	3.77	[7]

r-Cu/Ga_2O_3-SAM	0.3 M Na_2SO_4+ 20 mM $NaNO_3$	0.4	Ni form	-1.05	95.48	6.46	[8]
CuO@MnO_2/CF	0.5 M K_2SO_4+200mg·L^{-1} KNO_3−N)	/	Cu form	-0.645	94.92	4.08	[9]
Fe_1/NCB_n	100 mg L^{-1} NO_3^--N+50 mM Na_2SO_4	/	free-standing	-0.5	86.4	0.029	[10]
Cu/Cu_2O NWAs	0.5 M Na_2SO_4 + 200 ppm KNO_3	/	Cu mesh	4.318	95.8	-0.85	[11]
Pd octohedra	0.1 M Na_2SO_4 + 0.1 M $NaNO_3$	/	CP	9.33	79.9	-0.7	[12]

Tab. S6 Energy consumption comparison between electrolysis and Haber-Bosch process

Method	E_{elec} (kWh kg^{-1}_{NH3})
This work (electrolysis)	≈12.1
Haber-Bosch process	≈9-12

Using the optimal condition of -0.9 V vs. RHE (FE=93.5%, yield=7.62 mg h^{-1} cm^{-2}), we calculated the electrical energy consumption (E_{elec}) required to produce a unit mass of NH_3 using the following formula:

$$E_{elec}\left(kWh\ kg_{NH_3}^{-1}\right) = \frac{n \times F \times |E|}{\eta_{FE} \times M_{NH_3}} \times \frac{1}{3.6 \times 10^6}$$

where n=8; F is the Faraday constant; E is the applied potential (vs. RHE); ηFE is the FE; and M_{NH3} is the molar mass of NH_3.

The calculated E_{elec} is approximately 12.1 kWh kg^{-1}_{NH3}.

References:

1. X. Zheng, J. Hao, Z. Zhuang, Q. Kang, X. Wang, S. Lu, F. Duan, M. Du and H. Zhu, *Nanoscale*, 2024, 16, 4047-4055.
2. R. Jia, Y. Wang, C. Wang, Y. Ling, Y. Yu and B. Zhang, *ACS Catal.*, 2020, 10, 3533-3540.
3. M. Yang, T. Wei, J. He, Q. Liu, L. Feng, H. Li, J. Luo and X. Liu, *Nano Res.*, 2024, 17, 1209-1216.
4. X. Zhang, C. Wang, Y. Guo, B. Zhang, Y. Wang and Y. Yu, *J. Mater. Chem. A*, 2022, 10, 6448-6453.
5. J. Zhong, H. Duan, M. Cai, Y. Zhu, Z. Wang, X. Li, Z. Zhang, W. Qu, K. Zhang, D. Han, D. Cheng, Y. Shen, M. Xie, E. Cortes and D. Zhang, *Angew. Chem., Int. Ed.*, 2025, 64, e202507956.
6. Z. Fan, C. Cao, X. Yang, W. Yuan, F. Qin, Y. Hu, X. Sun, G. Liu, Y. Tian and L. Xu, *Angew. Chem., Int. Ed.*, 2024, 63, e202410356.
7. Y. Zhu, H. Duan, C. G. Gruber, W. Qu, H. Zhang, Z. Wang, J. Zhong, X. Zhang, L. Han, D. Cheng, D. D. Medina, E. Cortés and D. Zhang, *Angew. Chem., Int. Ed.*, 2025, 64, e202421821.
8. B. Liu, H. Liu, S. Qiang, J. Dai, J. Yan, J. Yu, Y.-T. Liu and B. Ding, *Adv. Funct. Mater.*, 2026, e29295.
9. Y. Xu, Y. Sheng, M. Wang, T. Ren, K. Shi, Z. Wang, X. Li, L. Wang and H. Wang, *J. Mater. Chem. A*, 2022, 10, 16883-16890.
10. X. Wang, L. R. Winter, X. Wu, Y. Fan, Y. Zhao, J.-H. Kim and M. Elimelech, *Sci. Adv.*, 2025, 11, eads6943.
11. X. Gu, J. Zhang, S. Guo, Y. Zhang, L. Xu, R. Jin and G. Li, *J. Am. Chem. Soc.*, 2025, 147, 22785-22795.
12. Y. Han, X. Zhang, W. Cai, H. Zhao, Y. Zhang, Y. Sun, Z. Hu, S. Li, J. Lai and L. Wang, *J. Colloid Interface Sci.*, 2021, 600, 620-628.